# Research on the fatigue properties of sub-HAZs in the X80 pipe

Kai Xu[1], Gui Qiao[2], Jun Wang[2], Shi Zhang[2], and Furen Xiao[2]

[1]Yanshan University College of Materials Science and Engineering
[2]Yanshan University

May 5, 2020

**Abstract**

Pipeline transmission is one of the most important ways of oil and gas transportation, and its safety is majorly threatened by fatigue fracture that generally occurs in heat-affected zone (HAZ) adjacent to the welded joint of the pipeline. Therefore, studying the fatigue properties of HAZ is important. In this work, the microstructure and mechanical properties in the HAZ of a X80 pipe were accurately simulated by thermal simulation. The fatigue life and crack growth rate of typical sub-HAZ were tested. Results showed that the fine grain HAZ had the lowest strength and fatigue life. By contrast, the coarse grain HAZ had the highest strength, but its fatigue life was lower than that of the intercritical HAZ. Furthermore, the microstructure of each sub-HAZ and its effect on fatigue properties were discussed in detail. The results will reveal the effects of microstructure and mechanical properties on the service safety of pipeline transportation.

# Keywords: X80 welded pipe; heat-affected zone; fatigue property; microstructure

**Nomenclature**

$a$ = thermal diffusivity

AF = acicular ferrite

BM = base metal

COD = crack opening displacement

$da/dN$ = fatigue crack growth rates

EBSD = electron backscatter diffraction

GB = granular bainite

HAZ = heat-affected zone

HV = hardness Vickers

KAM = kernel average misorientation

LSAW = longitudinal submerged arc welding

M/A = martensite/austenite

PF = polygonal ferrite

$q/v$ = welding heat input

$r$ = radial distance from the heat source

$P = \sigma_{\text{mix}}/\sigma_{\text{max}}$

SEM = scanning electron microscope

SENB = single edge notch bending

STEM = scanning transmission electron microscope

t = heating time

$T$ = peak temperature

$T_0$ = pre-heat temperature

XRD = X-Ray Diffraction

$\Delta K$ = stress intensity factor of the crack tip

$\lambda$ = thermal conductivity

$\sigma_{\text{max}}$ = the maximum stress

$\sigma_{\text{mix}}$ = the minimum stress

## Introduction

The increasing demand for oil and gas has prompted the use of pipelines to transport oil and gas and stimulated the continuous development of high-strength pipeline steel to increase conveying efficiency[1-4]. Grade X80 pipeline steel has become the primary steel grade of pipeline transportation, such as in the second and third lines of the West–East Gas Pipeline and the newly constructed Gas Pipeline from Russia to China through the Eastern route [5-7]. During the long service, the transmission pipelines are often affected by alternating stress caused by switching machines and internal pressure fluctuation [8]. Consequently, the fatigue cracks may generate, propagate, and even fracture [9]. Therefore, the fatigue performance of the X80 pipes is substantially for the safe transportation of pipelines.

Fatigue cracks usually initiate at the area of stress concentration caused by defects or changes in dimensions, microstructure, and mechanical properties [10-12]. In transmission pipelines, the fatigue cracks mainly generate in the welded joint, especially, heat-affected zone (HAZ) because of the stress concentration caused by weld reinforcement and the difference of microstructure and properties among the weld metal, HAZ, and base metal (BM)[13,14]. In addition, the microstructure in the HAZ is different in different distance from the welded joint [15]. The HAZ is divided into different sub-HAZs, including coarse-grain HAZ (CGHAZ), fine-grain HAZ (FGHAZ), and intercritical HAZ (ICHAZ)[13]. Fatigue cracks mainly initiate in either the CGHAZ of the welded joints with retained weld reinforcement or in the FGHAZ of the welded joints after removing the weld reinforcement [16,17]. For the X80 pipes, the weld reinforcement in pipe body normally remains, but those of the two ends in the pipe must be removed to facilitate girth welding. Therefore, the possible regions of fatigue crack initiation on the X80 pipeline are in the CGHAZ and FGHAZ. For these reasons, the fatigue property of each sub-HAZ in the X80 pipeline needs further research.

The performance testing of each sub-HAZ is hindered due to their small areas. Thermal simulation can be used for each sub-HAZ to test their individual performance[18,19]. Although thermal simulation methods have been widely used to study the microstructure and mechanical properties of the HAZ[20,21], reports on the fatigue performance of the HAZ mainly focused on the overall weld joint [22,23]. Few works on the fatigue properties of each sub-HAZ in the X80 pipeline, especially in terms of the fatigue crack growth, are available[24]. In addition, the performance of ICHAZ has been rarely reported. As a region close to the BM

in the HAZ of the pipeline, ICHAZ still has properties different from that of the BM[25]. The extension of the fatigue crack at the weld joint of the pipeline also passes through the ICHAZ[23]. Therefore, the ICHAZ performance of the X80 pipeline should also be studied.

In this work, the three sub-HAZs of the X80 pipe were simulated by using a thermal simulation. The fatigue properties (including fatigue crack growth) of each sub-HAZ were evaluated. The microstructure of each region and its influence on performance were analyzed by using electron backscatter diffraction (EBSD) and scanning transmission electron microscope (STEM). The results can help to improve the safety of pipeline transportation.

# 2. Materials and methods

2.1 Materials

The materials in this study were cut from a commercial X80 longitudinal submerged arc welding (LSAW) pipe of the outer diameter of 1219 mm and wall thickness of 22 mm for the Third West–East Gas Transmission Pipeline Project. The material chemical composition is shown in **Table 1** . The microstructure and mechanical properties of HAZ are affected by the weld heat input [26]. Therefore, the microstructure and hardness of the weld joint of the LSAW pipe were first analyzed to obtain the reasonable simulation parameters as shown in **Fig. 1** . Different microstructures and hardness levels were found in the weld metal, HAZ, and BM (**Fig. 1a** ). The HAZ was clearly divided into CGHAZ, FGHAZ, and ICHAZ (**Figs. 1b** –**1d** ). The lowest hardness appears in FGHAZ **(Fig. 1a** ). Therefore, the three typical sub-HAZs of CGHAZ (Region 1), FGHAZ (Region 2), and ICHAZ (Region 3) were selected to evaluate the effect of HAZ on fatigue properties of the X80 LSAW pipe.

**Table 1.** The chemical composition of the X80 LSAW pipe (wt.%).

| C | Mn | Si | P | S | Mo | Ni | Cr | Cu | Nb | Ti | Al |
|------|------|------|-------|-------|-------|-------|-------|-------|-------|-------|-------|
| 0.06 | 1.75 | 0.24 | 0.011 | 0.002 | 0.005 | 0.018 | 0.224 | 0.022 | 0.070 | 0.016 | 0.041 |
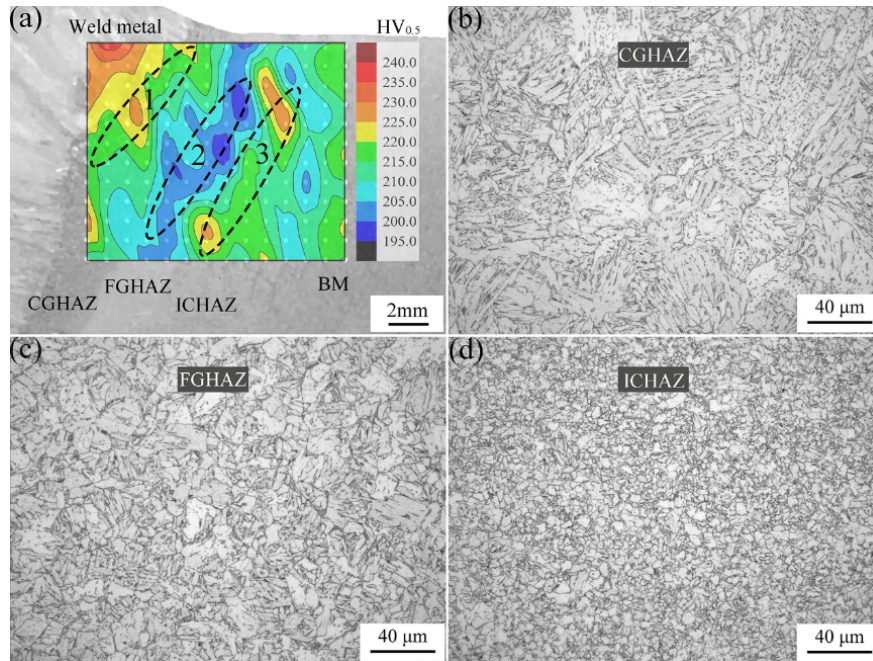
**Fig. 1** (a) The hardness distribution diagram and (b–d) the microstructure of each sub-HAZs in the real HAZ of the X80 pipeline.

2.2 Thermal simulation

Welding thermal simulation test was performed on a Gleeble-3800 thermal simulator. The welding heat cycle processes with different peak temperatures are shown in **Fig. 2a** , and the hardness of simulated specimens is shown in **Fig. 2b** . The peak temperature at different distances from the weld metal was calculated from the following formula to obtain the similar microstructure and mechanical properties in sub-HAZs of the X80 pipe [15]:

$$T - T_0 = \frac{\frac{q}{v}}{2\pi\lambda t} \exp\left(-\frac{r^2}{4at}\right), (1)$$

where the $T$ is the peak temperature and $T_0$ is the preheat temperature in the different sub-HAZs, $\frac{q}{v}$ is the welding heat input, t is the heating time, $\lambda$ is the thermal conductivity, $r$ is the radial distance from the heat source, and $a$ is the thermal diffusivity.

Calculation results showed that the peak temperatures of 1320 °C, 1020 °C, and 880 °C corresponded to typical sub-HAZs of CGHAZ (Region 1), FGHAZ (Region 2), and ICHAZ (Region 3), respectively. The change rule of the hardness in the simulated specimens was similar to the distribution in the HAZ of the weld joint of X80 pipe (**Figs. 2b** and **1a** ), and the hardness of the simulated specimens with peak temperatures of 1320 °C, 1020 °C, and 880 °C was similar to the Regions 1, 2, and 3 in the actual sub-HAZ of X80 pipe. Therefore, the simulated specimens with peak temperatures of 1320 °C, 1020 °C, and 880 °C were selected to represent Regions 1, 2, and 3, respectively, in evaluating the effect of HAZ on the fatigue properties of X80 LSAW pipe.
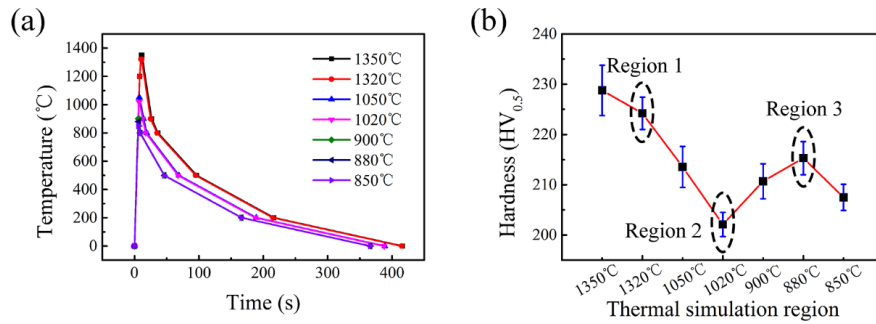


**Fig. 2** (a) Thermal simulation processes with different peak temperatures, and (b) the hardness of the thermal simulation region of X80 pipe.

2.3 Fatigue tests

The fatigue properties of the simulated sub-HAZ specimens were studied on an MTS servo-hydraulic universal testing machine. The fatigue life and crack propagation were tested. The geometry of fatigue life specimens is shown in **Fig. 3a** . According to the service condition of the pipeline, the tension-tension fatigue with a stress ratio ($R = \sigma_{mix}/\sigma_{max}$) of 0.1 was adopted, and the maximum stress of 550 MPa was selected for the reason that the minimum yield strength of the X80 pipeline steel was 550 MPa. A sinusoidal wave of 30 Hz was used for all of the fatigue tests. Each fatigue specimen was examined until a fracture was formed. The total fatigue cycles were counted as the fatigue life. Single edge notch bending (SENB) samples were used for the fatigue crack growth test according to the GB/T6389-2017. The tests were initiated with fatigue precracking, which was generated by cyclic loading until a crack with the desired length was formed, to initiate an initial crack from the sharp notch of each SENB specimen as shown in **Fig. 3b** . The crack length was recorded by using a crack-opening displacement extensometer.

4
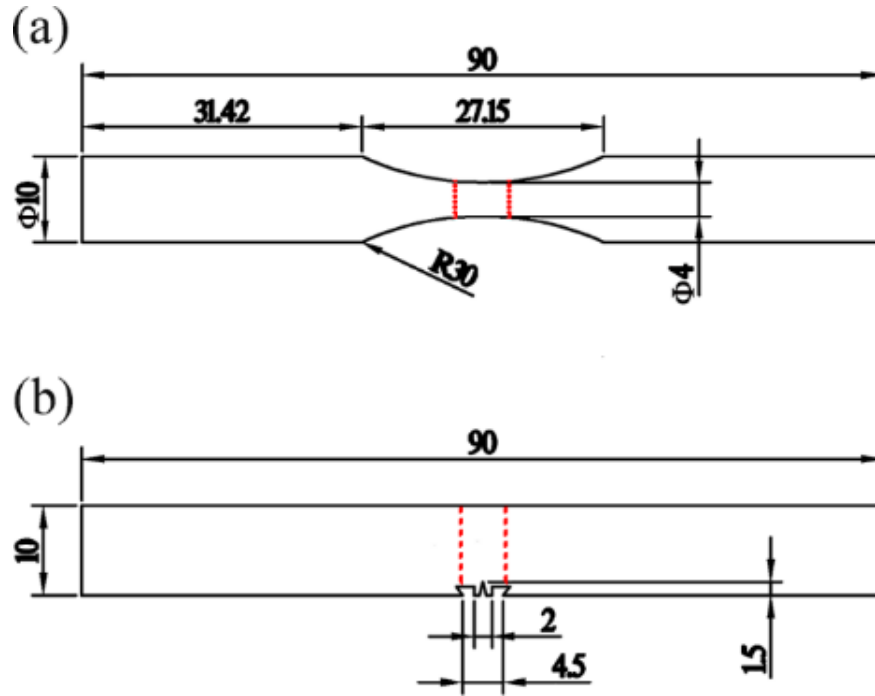
**Fig. 3** The geometry of the specimens used in the study (all dimensions are in mm): (a) the sample of the fatigue life test, and (b) SENB sample of fatigue crack growth test.

2.4 Fracture and microstructure analysis

After the performance test was completed, the fracture morphology was observed by using a Hitachi S-3400N scanning electron microscope (SEM), and the fracture causes were analyzed. The grain size, orientation, and microscopic strain in each sub-HAZs were analyzed by EBSD. The microstructure in each region was observed by using a Talos F200X STEM. The influencing factors of performance changes in different regions were analyzed through these microscopic observations.

# 3. Results

3.1 Tensile and fatigue properties

The fatigue resistance of steel is related to strength[27,28]. **Figures 1a** and **2b** show the different hardness levels in the sub-HAZs, which imply their different strengths that may affect the fatigue life. Thus, the tensile properties of the three regions in HAZ of the X80 steel were measured.**Figure 4** shows the engineering stress–strain curves of the three regions in HAZ of the X80 steel, and the typical mechanical properties are listed in **Table 2** . Region 1 (CGHAZ) had the highest strength and lowest elongation, whereas Region 2 (FGHAZ) had the lowest strength and the highest elongation. The yield strength was close to the 550 MPa specified by API 5L specification. The strength and elongation of Region 3 (ICHAZ) were between Regions 1 and 2. These results are consistent with the hardness distribution in the weld joint of the X80 LSAW pipe (**Fig. 1a** ) and the simulated specimens of sub-HAZs (**Fig. 2b** ) and also verify that heat simulation can provide similar microstructure and mechanical properties for the different sub-HAZs.
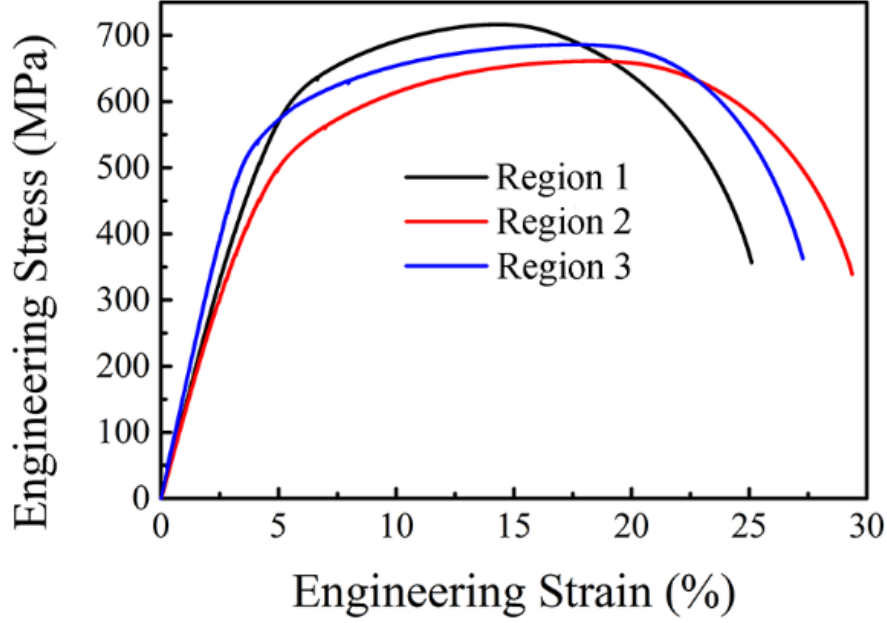
**Fig. 4** The engineering stress-strain curves of each region of the X80 pipe.

**Table 2** . The mechanical properties of each region of the X80 pipe.

| Region | Yield strength (MPa) | Tensile strength (MPa) | Total elongation (%) |
|---|---|---|---|
| 1 | 605.8 | 716.7 | 22.52 |
| 2 | 552.16 | 663.16 | 26.33 |
| 3 | 583.56 | 688.71 | 24.88 |

**Figure 5** shows the results of fatigue life and crack propagation curves of the three simulated regions, and **Fig. 5a** shows that Region 2 represents the lowest fatigue life, which may be related to its low strength. However, Region 1 has higher strength than Region 3, but its fatigue life is lower than that of Region 3. These results indicate that other factors in addition to strength affect the fatigue life of X80 steel sub-HAZs. The fatigue life of the steels includes the cycles of fatigue crack initiation, propagation, and fracture[29]. Fatigue crack propagation is used as a basis to predict fatigue life. Therefore, the fatigue crack growth rates ($da$ /$dN$ ) were measured. **Figure 5b** shows the relationship of $da$ /$dN$ with a stress intensity factor of the crack tip ($\Delta K$ ). The fatigue crack growth rates of the three regions in HAZ showed a similar rule that $da$ /$dN$ increased with $\Delta K$ . When $\Delta K$ was greater than 30 MPa[?]m$^{1/2}$, the fatigue crack exhibited stable propagation. The relationship of $da$ /$dN$ and $\Delta K$ conformed to the Paris equation expressed as follows [30]:

$$da /dN = C [?]\Delta K^m , (2)$$

where $C$ and $m$ are constants with materials.

6
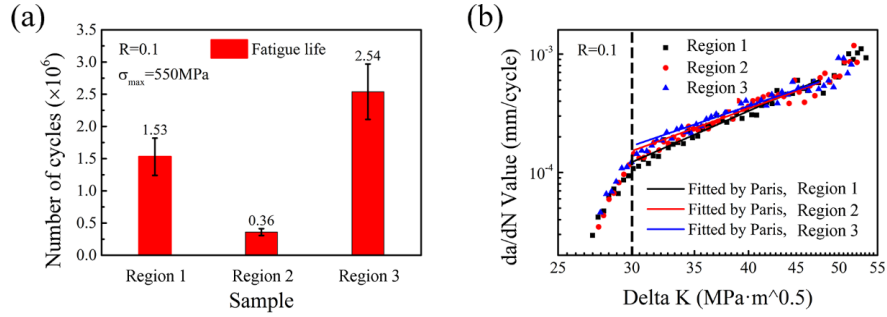
**Fig. 5** (a) Fatigue lives and (b) fatigue crack growth curves in each region of the X80 pipe.

**Table 3** . The results of the fitting Paris formula in each region of the X80 pipeline.

| Region | $C$ | $m$ |
|---|---|---|
| 1 | $9.66\times10^{-10}$ | 3.45 |
| 2 | $8.94\times10^{-9}$ | 2.86 |
| 3 | $1.8\times10^{-8}$ | 2.68 |

The constants of $C$ and $m$ in Eq. (2) of the three regions are listed in **Table 3** . Results show that Region 3 had a high crack growth rate, and Region 1 had a low crack growth rate when the fatigue crack just reached the stable propagation zone. However, when the fatigue crack was in stable propagation zone, the fastest and slowest increases were observed for the crack growth rates of Regions 1 and 3, respectively. Consequently, the fatigue crack growth rate in the three regions had the same value when $\Delta K$ reached 44.58 MPa[?]m$^{1/2}$. The difference in fatigue crack growth rate of three regions in HAZ may be related to the microstructural sensitivity of fatigue crack propagation behavior.

3.2 Fatigue fracture observations

The typical fractography of the three regions in HAZ after fatigue fracture at the maximum stress of 550 MPa is shown in **Fig. 6** . The fracture surface contained two clear sections, namely, the "flat fracture" and final "ductile fracture" sections. The "flat fracture" section corresponded to the typical fatigue failure, which included the fatigue crack initiation and propagation. The fatigue crack initiation and propagation were the most important processes that determine fatigue endurance. The "ductile fracture" section was considered a quasistatic fracture when the bearing capacity of specimens was less than the maximum cyclic loading because fatigue crack propagation reduced the loading area (**Figs. 6a–6c**) .
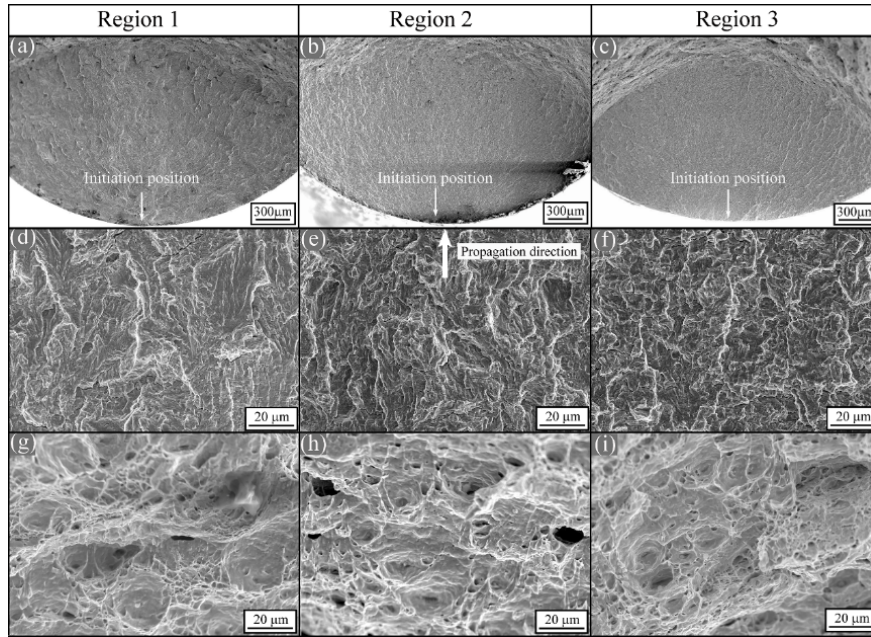
**Fig. 6** Observation of the fatigue fracture in each region by SEM: (a–c) macroscopic fracture, (d–f) crack propagation zone and (g–i) final rupture zone.

In the "flat fracture" section, the fatigue cracks of the three regions in HAZ initiated at a small dot scope on the specimen surface and propagated toward the center in radial directions, which were clearly displayed by the river pattern. No obvious defects were observed in the crack initiation region (**Figs. 6a–6c** ). In the fatigue crack propagation zone (**Figs. 6d–6f** ), the microfracture surfaces were uniform and contained transgranular cleavage facets and rough relief but no clear fatigue striations. Certain secondary cracks caused by microtear were found on the fracture surface. However, some distinctions were observed in the fracture surfaces of three regions in HAZ. The facet size, secondary crack size, and amount on the fracture surface of Region 1 were larger than those of Regions 2 and 3, with Region 3 having the smallest facet. The different fracture characteristics presented between the different regions in HAZ may be related to the variation in the microstructure. In the "ductile fracture" section (**Figs. 6g–6i** ), the dimples were filled throughout the crack final fracture zones of all the specimens. The dimples of Region 1 were large and shallow, whereas those of Region 2 were small and deep. These results are consistent with the results of elongation. Region 2 had a high elongation (**Fig. 4** and**Table 2** ).

3.3 Microstructure

**Figure 7** shows the microstructure of the three regions in HAZ after the welding thermal cycle with different peak temperatures. Compared with that in **Fig. 1** , the microstructure of simulated HAZ specimens was similar to the HAZ of the X80 LSAW pipe. At the peak temperature of 1320 °C, the microstructure of Region 1 was dominated by granular bainite (GB). Many dark film- and rod-like constituents were distributed in the bainite ferrite matrix, and prior-austenite grain boundary was clearly visible (**Fig. 7a** ). The X-Ray Diffraction (XRD) pattern illustrated that the microstructure consisted of main BCC $\alpha$-phase and few FCC $\gamma$-phase (**Fig. 8** ). The $\gamma$-phase retained austenite because the bainite was an incomplete transformation accompanied by martensite and retained austenite [31]. Therefore, the dark film- and rod-like constituents distributed in the bainite ferrite matrix were martensite/austenite (M/A) islands, which can be confirmed by the STEM microstructure of the three regions in HAZ shown in**Fig. 9a** . The ferrite was mainly non-equiaxial with lots of entangled dislocations. Some film-like and small dot-like M/A constituents were distributed at the non-equiaxial ferrite grain boundaries, and some large bulk M/A constituents were distributed at the corner between the non-equiaxial ferrite grains (**Fig. 9a** ). Although the peak temperature reached 1320 °C

for CGHAZ, the prior-austenite grain size was still lower than 60 μm (**Fig. 7a** ). The small prior-austenite grain size may be attributed to the undissolved Ti and Nb carbonitride precipitates, which considerably restrained the austenite grain growth [32].
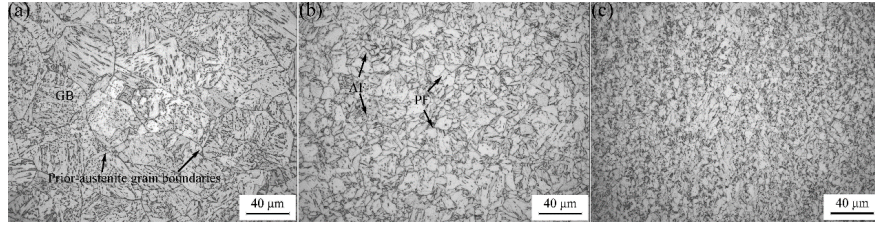


**Fig. 7** The metallographic observation of each simulated sub-HAZ of the X80 pipeline: (a) region 1, (b) region 2, and (c) region 3.
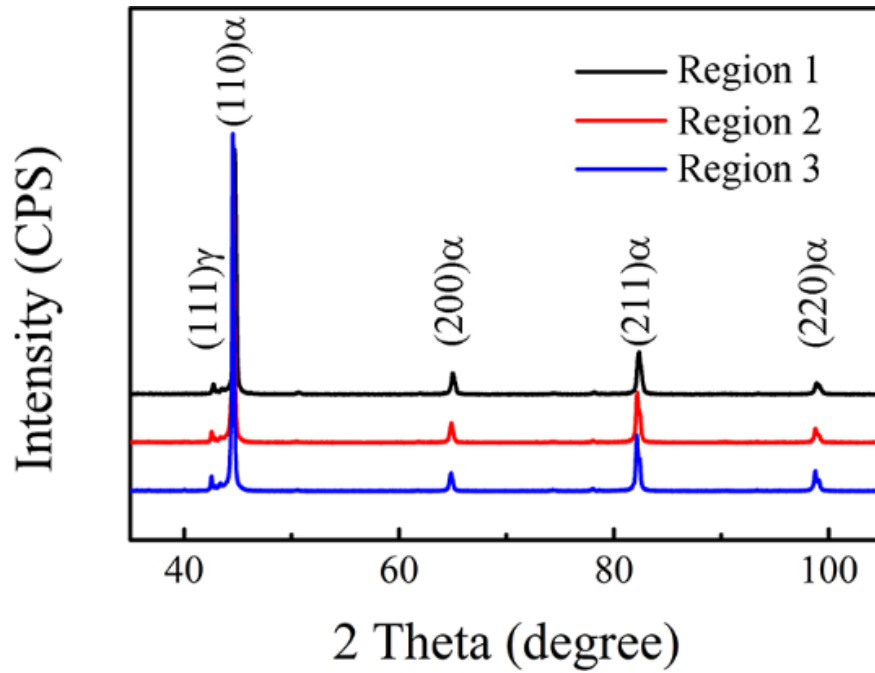


**Fig. 8** The XRD patterns of the three regions of the X80 pipe.
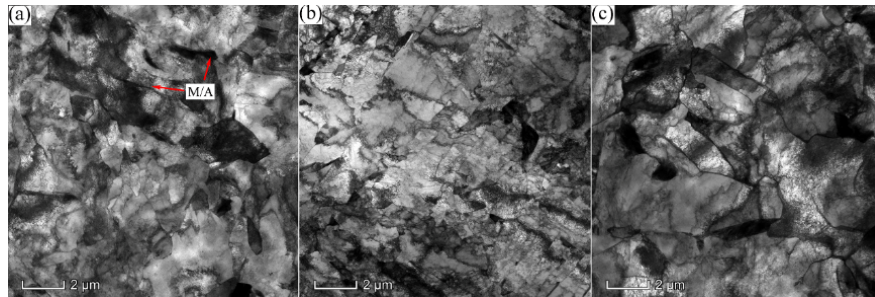


**Fig. 9** Microstructure observation in three regions of the X80 pipe by STEM: (a) region 1, (b) region 2,

and (c) region 3.

When the peak temperature decreased to 1020 °C, the microstructure of Region 2 appeared to consist of main acicular ferrite (AF) and polygonal ferrite (PF), and the size of the AF and PF grains and the amount of M/A constituents decreased (**Fig. 7b** ). STEM micrograph shows that the ferrite grain was fine. Some fine dot-like M/A constituents were distributed in the ferrite grain or at ferrite grain boundaries (**Fig. 9b** ). When the peak temperature decreased to 880 °C, variation in the microstructure of Region 3 was observed (**Fig. 7c** ). The microstructure was refined and consisted of fine PF and AF. Moreover, the amount and size of the M/A constituents increased (**Fig. 9c** ).

3.4 EBSD analysis

**Figure 10** shows the crystallographic characteristics of the three regions in HAZ using EBSD. The image quality maps showed that the microstructure of Region 1 with the peak temperature of 1320 °C mainly consisted of lath and fine granular ferrites, and the prior-austenite grain boundary was clearly visible (**Fig. 10a** ). The microstructure was GB in accordance with the metallographic observation (**Fig. 7a** ). With the decrease in the peak temperature to 1020 °C (for Region 2), the microstructure changed to fine AF and massive ferrite, and the prior-austenite grain boundary disappeared (**Fig. 10b** ). When the peak temperature further decreased to 880 °C (for Region 3), the microstructure changed remarkable and it mainly contained fine granular ferrite (**Fig. 10c** ). The maps of grain orientation (**Figs. 10d–11f** ) and grain boundary misorientation distribution (**Figs. 10g–10i** ) indicated that the grain boundaries between the lath ferrite or AF in the specimens of Regions 1 and 2 were mainly low-angle boundaries (**Figs. 10d–10e and10g–10h** ). The fine massive or granular ferrites in the specimens of Regions 2 and 3 were mainly high-angle boundaries (**Figs. 10e–10f** and **Figs. 10h–10i** ). The grain orientation changes mainly occurred between high-angle grain boundaries. In addition, the kernel average misorientation (KAM) maps in the three regions of HAZ are also calculated and shown in **Figs. 10j–10l** . The KAM map is used to evaluate the microscopic strain[33,34]. Comparing **Figs. 10j–10l** with**Figs. 10h–10i** , the microscopic strain mainly concentrated in areas with low-angle grain boundaries. Thus, the generation of microscopic strain may relate to the transformation of bainite ferrite and M/A islands. Consequently, the microscopic strain in the sub-HAZs decreased with the peak temperature.

According to the results of EBSD analysis in **Fig. 10** , the distributions of the misorientation angle and effective grain size were statistically analyzed and are illustrated in **Fig. 11** . The fraction of the misorientation angle for Region 1 mainly concentrated on low angle, its effective grain size was large, and the average effective grain size reached 14.1 μm. With the decrease in peak temperature, the fraction of the low-angle grain boundaries also decreased, but that of the high-angle grain boundaries increased. Consequently, the average effective grain size decreased to 7.71 μm for Region 2 and 3.9 μm for Region 3.
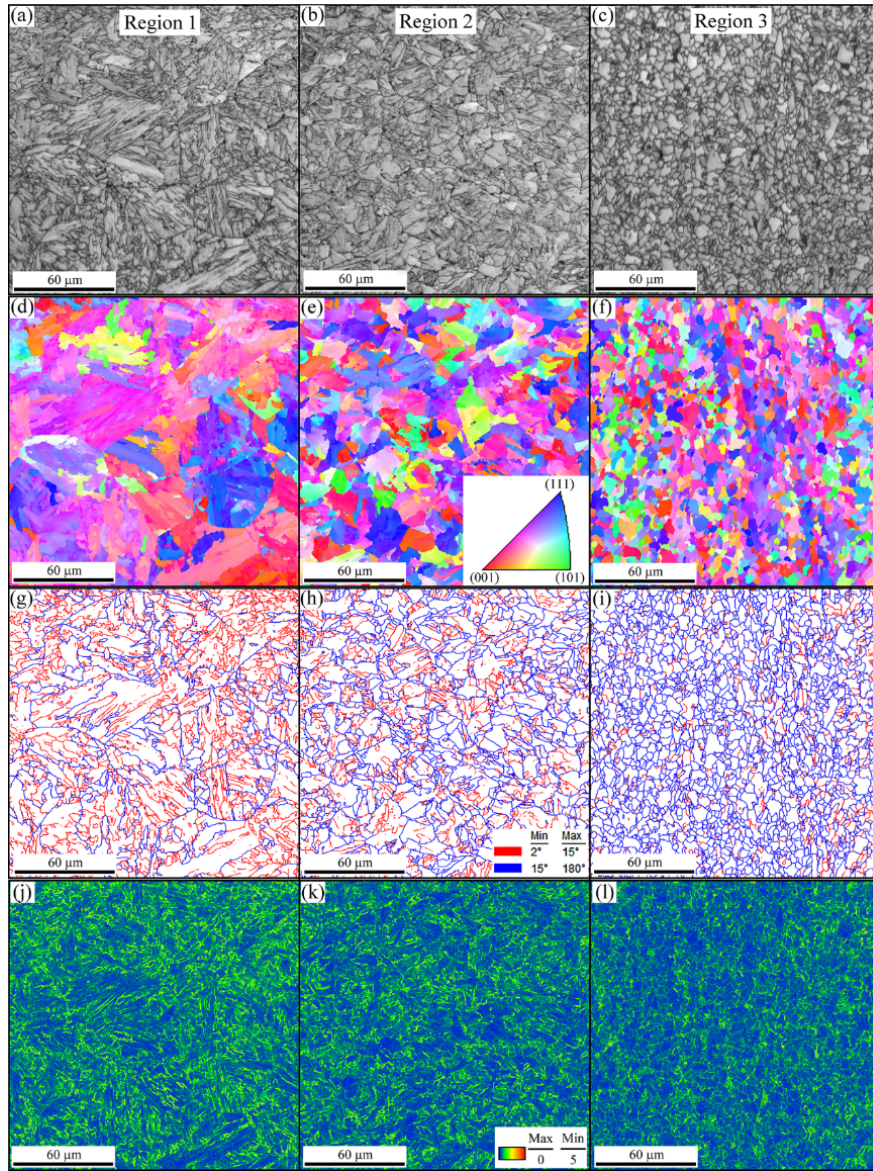
**Fig. 10** EBSD analysis of each region of the X80 pipe: (a–c) image quality maps, (d–f) grain orientations maps, (g–i) grain boundaries maps, and (j–l) kernel average misorientation maps.
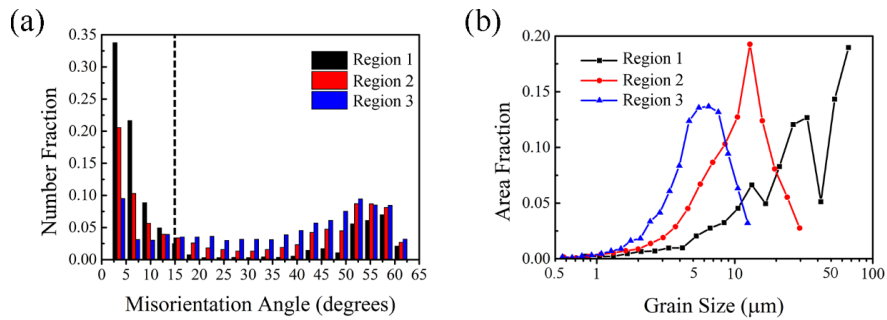
**Fig. 11** (a) the misorientation angle and the fraction of grain boundaries, and (b) the size and the fraction of the grains in the three regions of the X80 pipe.

## 4. Discussion

The distribution of hardness in the weld joint of the X80 LSAW pipe showed a weakened region in FGHAZ (**Fig. 1a** ), which conformed to the results of welding thermal simulation shown in **Figs. 2b** and**4** . Low hardness and strength occurred when the peak temperature was 1020 °C (**Figs. 2b** and **4** ). Therefore, the region showed the low fatigue life (**Fig. 5a** ) because the fatigue life strongly depended on the strength [27,28]. Although the strength of Region 3 (ICHAZ) was lower than that of Region 1 (CGHAZ), the former had the highest fatigue life. The change of mechanical properties in sub-HAZs of the weld joint could be ascribed to the difference of microstructure (**Figs. 7–10** ) because of the effects of peak temperature on phase transformation during the welding heat cycle.

**Figure 12** illustrates the thermal expansion curves of the specimens during the simulated welding heat cycle. The phase transformation temperatures of $A_{c1}$ and $A_{c3}$ during heating were as high as 830 °C and 1026 °C, respectively. When the peak temperature reached 1320 °C, the austenite transformation was completed during heating, and the austenite grain quickly developed in the heating temperature from 1026 °C to 1320 °C. Thus, only one phase transformation of GB occurred in the range of temperature from 630 °C to 500 °C. The final microstructure was mainly granular bainite GB (**Fig. 7a** ). When the peak temperature decreased to 1020 °C, the austenite transformation was almost complete, and the fine and inhomogeneous austenite microstructures were obtained. Two phase transformations, namely, ferrite phase transformation from 800 °C to 660 °C and AF (or bainite) phase transformation from 660 °C to 510 °C, were observed in the dilatometric curve during cooling. Thus, the mixture microstructure of ferrite and AF (or bainite) was obtained (**Fig. 7b** ). With further decrease in the peak temperature to 880 °C, only a part of austenite was formed during heating. During cooling, the ferrite phase transformation first occurred from 800 °C to 670 °C, and then the AF (or bainite) occurred from 670 °C to 500 °C. Some parts of the tempering as-rolled microstructure remained. Therefore, the finely mixed microstructure consisting of AF (or bainite), ferrite, and tempered as-rolled microstructure was obtained (**Fig. 7c** ).



12
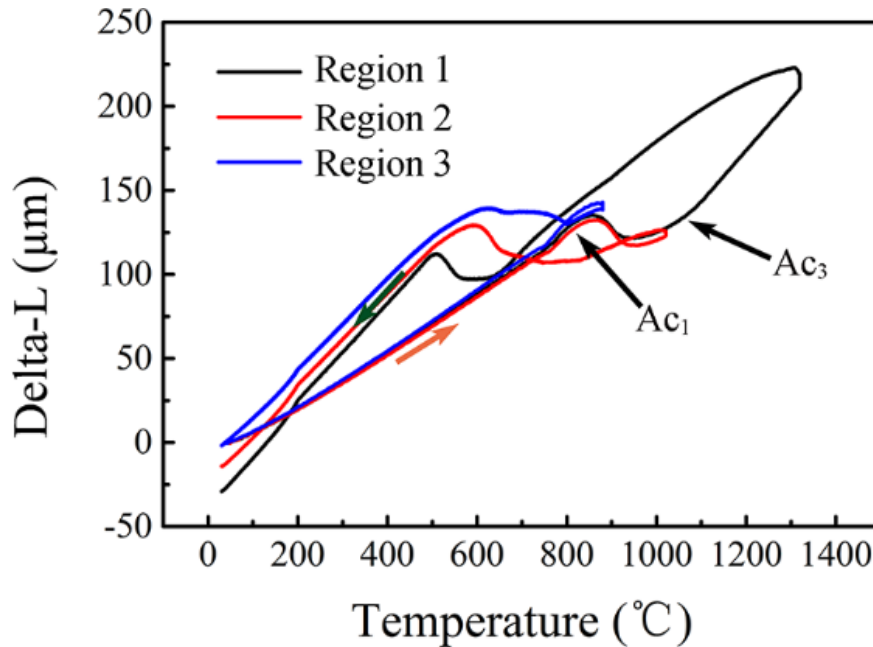
**Fig. 12** The curves of volume changes in three regions during the thermal simulation.

The difference of final microstructure in sub-HAZs was caused by the welding heat cycle with peak temperature results in its different mechanical properties. In Region 1, the microstructure was dominated by GB, which consisted of fine lath-like bainite ferrite (**Figs. 7a** and**10a** ) and M/A islands (**Figs. 7a** and **9a** ), and high density dislocation existed in the lath-like bainite ferrite (**Fig. 9a** ). Therefore, the high strength and hardness were obtained (**Figs. 2b** and **4** ). In Region 2, the part PF existed in the final microstructure (**Fig. 7b** ), and the amount of sub-microstructure and M/A islands decreased (**Figs. 9b** and**10b** ), resulting in low strength and hardness appearing in these sub-HAZs (**Figs. 2b** and **4** ). Although a part of PF also existed in the final microstructure (**Fig. 7c** ), the amount of M/A islands in Region 3 increased, and some tempering as-rolled structures remained (**Figs. 7c** and **9c** ); thus, the higher strength and hardness were obtained.

Fatigue fracture is a process of crack initiation, propagation, and ultimate fracture, and fatigue life mainly includes fatigue crack initiation life and crack propagation life [29]. Therefore, all factors that affect the fatigue crack initiation and propagation will affect the fatigue life. Considerable research reports that the fatigue resistance of the metals relates to the strength [27,28]. The fatigue cracks generally generate on the surface of specimens. For smooth specimens, the surface local slipping under cyclic stress is one of the most important factors to affect fatigue crack initiation. The surface local slipping strongly depends on the maximal cyclic stress and strength of the materials. In this work, the strength of Region 2 is the lowest (**Table 2** ), and the yield strength is only 552.2 MPa, which is near to the maximum stress of 550 MPa. The large strain is generated under cyclic stress. Consequently, Region 2 has the lowest fatigue life, with only $3.6 \times 10^5$ cycles (**Fig. 5a** ). From the point of view of the relationship between fatigue resistance with the strength of materials, Region 1 that has the highest yield strength of 605.8 MPa will have the highest fatigue life. However, the fatigue life of Region 1 is only $1.53 \times 10^6$ cycles and lower than the Region 3 of $2.54 \times 10^6$ cycles (**Fig. 5a** ), though the yield strength of Region 3 is 583.6 MPa. The fatigue crack initiation and propagation are sensitive to the microstructure [35,36]. The microstructure of Region 1 is coarse GB, and large M/A islands are distributed in the microstructure (**Figs. 7a** and **9a** ). The stress concentration occurs at the interface of the M/A islands under cyclic fatigue stress because of the large difference of strength between M/A islands and the bainite ferrite matrix [37]. Thus, the fatigue crack initiation will be facilitated, and the fatigue crack initiation life decreases. The microstructure for Region 3 consists of PF, AF (or bainite), and tempering as-rolled microstructure, and many M/A islands are distributed in the matrix (**Figs. 7c** and**9c** ). The microstructure is fine and uniform (**Fig. 10c** ), and the average effective grain size is only 3.9 μm (**Fig. 11b** ). The fine and uniform microstructure can decrease the local stress concentration, which retards the fatigue crack initiation and increases the fatigue crack initiation life.

In addition, the microstructure in different sub-HAZs also affects the behavior of fatigue crack propagation [35]. As shown in**Fig. 6** , the fatigue fracture shows the transgranular cleavage facets and rough relief. Comparison of fatigue fractography (**Fig. 6** ) and microstructure (**Figs. 7** and **10** ), revealed that the size of transgranular cleavage facets is close to the effective grain size. The fatigue crack propagation is transgranular rupture, and the high-angle grain boundaries can effectively restrain fatigue crack propagation, whereas the low-angle grain boundaries have minimal effect on fatigue crack propagation [38]. The effect of microstructure on fatigue crack propagation can be clearly confirmed by the microstructure observation of the fatigue crack section. **Figure 13** shows the maps of grain orientation along the fatigue crack section close to the crack initiation area. In Region 1, the fatigue crack propagation passes directly through the coarse bainite grain, and the subgrain boundaries with low-angle grain orientation have little effect on the orientation of fatigue crack propagation. Therefore, some small changes of orientation occur in the subgrain boundaries (**Fig. 13a** ). The behavior of fatigue crack propagation may be attributed to the structure of bainite lath boundaries. STEM results show that the M/A islands are mainly massive and distributed in at the corner between the bainite grains. Therefore, the fatigue fracture surface of Region 1 shows coarse transgranular cleavage facets and some secondary cracks (**Figs. 6a** and**6d** ). This result indicates that the microstructure has high increase in fatigue crack propagation rate (**Fig. 5b** and**Table 3** ) and low fatigue crack propagation life. When the microstructure is refined and the high-angle grain boundaries increases,

13

the orientation of fatigue crack propagation is changed, its path is affected (**Figs. 13b** and **13c)** , and its rate is slowed down, thus increasing the crack propagation life.

The microstructure and mechanical properties in HAZ differ from those in sub-HAZs due to the effect of the peak temperature on phase transformation and final microstructure. In FGHAZ, ferrite transformation occurs during the cooling of the welding thermal cycle, which weakens the sub-HAZ. Under high cyclic stress, the high local strain facilitates fatigue crack initiation in FGHAZ and decreases the fatigue life. Therefore, the fatigue performance of the two ends in the pipeline where the weld reinforcements are removed must be prioritized.**Fig. 1** shows that the fatigue crack of the weld joint of X80 LSAW pipe initiates in either CGHAZ or FGHAZ, and its path must pass through the other sub-HAZs and BM. Therefore, studying the fatigue life of simulated welding HAZ is beneficial to analyze the behavior of fatigue crack initiation and propagation in sub-HAZs but cannot fully reflect the fatigue life for the actual welded joint of X80 LSAW pipe. Determining the fatigue behavior of welding HAZ combined with full-thickness specimens of the weld joint can contribute in the research and prediction fatigue life of the weld joint of X80 LSAW pipe.
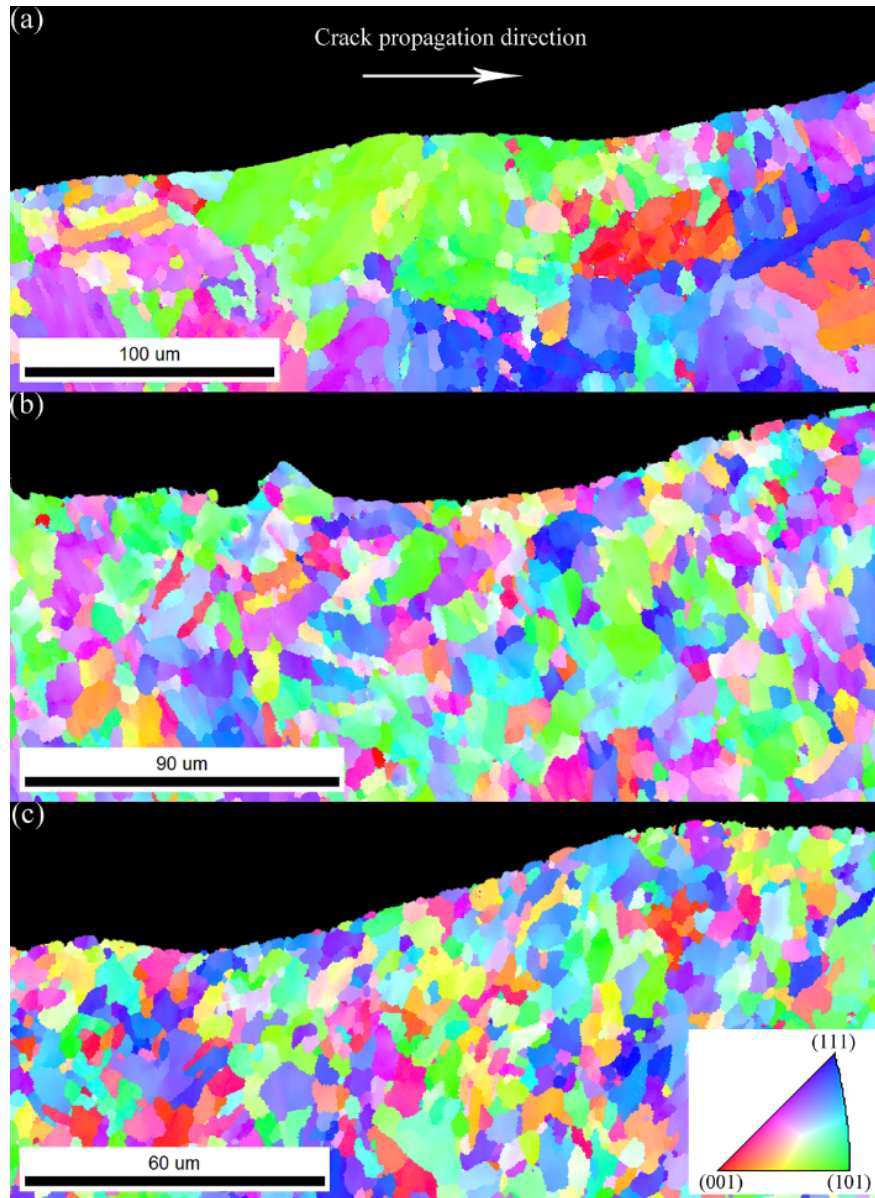
**Fig. 13** Grain orientations near the fatigue cracks in the three regions of the X80 pipe: (a) Region 1, (b) Region 2, and (c) Region 3.

## 5. Conclusion

In this work, the HAZ of the X80 pipe was simulated by the thermal simulation test. The changes in microstructure of each sub-HAZ during welding were discussed, and the fatigue performance of each sub-HAZ was determined. The conclusions are as follows:

(1) The final microstructure in the CGHAZ is mainly granular bainite; the FGHAZ has the mixture microstructure of polygonal ferrite and acicular ferrite (or bainite); the finely mixed microstructure in the ICHAZ consisted of acicular ferrite (or bainite), ferrite and tempered as-rolled microstructure.

(2) CGHAZ has the highest strength, but its fatigue life is lower than that of the ICHAZ because the stress concentration occurs at the interface of the M/A islands, and its crack growth rate increases rapidly. The uniform and fine microstructure improves the fatigue life of intercritical HAZ.

(3) FGHAZ has the lowest fatigue life because it has the lowest strength. Therefore, the effect of the weakness of strength and fatigue properties in FGHAZ on the pipeline service safety must be considered.

# Acknowledgements

**Reference**

1. Dong S, Zhang Lb, Zhang H, Chen Y, Zhang H. Experimental study of unstable crack propagation velocity for X80 pipeline steel.*Fatigue & Fracture of Engineering Materials & Structures.*2019;42(4):805-817.

2. Kingklang S, Uthaisangsuk V. Micromechanical modeling of anisotropic behavior of pipeline steel grade X65. *Materials & Design.*2017;127:243-260.

3. Shi X, Yan W, Xu D, et al. Microbial corrosion resistance of a novel Cu-bearing pipeline steel. *Journal of Materials Science & Technology.* 2018;34(12):2480-2491.

4. Zhang H, Liang Y, Ma J, Shen Y, Yan X, Yuan M. An improved PSO method for optimal design of subsea oil pipelines. *Ocean Engineering.*2017;141:154-163.

5. An T, Zhang S, Feng M, et al. Synergistic action of hydrogen gas and weld defects on fracture toughness of X80 pipeline steel.*International Journal of Fatigue.* 2019;120:23-32.

6. Zhang L, Shen H, Lu K, et al. Investigation of hydrogen concentration and hydrogen damage on API X80 steel surface under cathodic overprotection. *International Journal of Hydrogen Energy.*2017;42(50):29888-29896.

7. Zheng Y, Zhang L, Shi Q, Zhou C, Zheng J. Effects of hydrogen on the mechanical response of X80 pipeline steel subject to high strain rate tensile tests. *Fatigue & Fracture of Engineering Materials & Structures.* 2020;43(4):684-697.

8. Giorgetti V, Santos EA, Marcomini JB, Sordi VL. Stress corrosion cracking and fatigue crack growth of an API 5L X70 welded joint in an ethanol environment. *International Journal of Pressure Vessels and Piping.* 2019;169:223-229.

9. Amaro RL, Drexler ES, Slifka AJ. Fatigue crack growth modeling of pipeline steels in high pressure gaseous hydrogen. *International Journal of Fatigue.* 2014;62:249-257.

10. Benjamin Britton T, Wilkinson AJ. Stress fields and geometrically necessary dislocation density distributions near the head of a blocked slip band. *Acta Materialia.* 2012;60(16):5773-5782.

11. Fischer C, Fricke W, Rizzo CM. Fatigue tests of notched specimens made from butt joints at steel. *Fatigue & Fracture of Engineering Materials & Structures.* 2016;39(12):1526-1541.

12. Stiénon A, Fazekas A, Buffière JY, Vincent A, Daguier P, Merchi F. A new methodology based on X-ray micro-tomography to estimate stress concentrations around inclusions in high strength steels.*Materials Science and Engineering: A.* 2009;513-514:376-383.

13. Veerababu J, Goyal S, Sandhya R, Laha K. Low cycle fatigue behaviour of Grade 92 steel weld joints. *International Journal of Fatigue.*2017;105:60-70.

14. Wang B, Duan QQ, Yao G, et al. Fatigue fracture behaviour of spot welded B1500HS steel under tensile-shear load. *Fatigue & Fracture of Engineering Materials & Structures.* 2015;38(8):914-922.

15. Kim S, Kang D, Kim T-W, Lee J, Lee C. Fatigue crack growth behavior of the simulated HAZ of 800MPa grade high-performance steel.*Materials Science and Engineering: A.* 2011;528(6):2331-2338.

16. Schork B, Kucharczyk P, Madia M, et al. The effect of the local and global weld geometry as well as material defects on crack initiation and fatigue strength. *Engineering Fracture Mechanics.*2018;198:103-122.

17. Tian P, Xu K, Lu G-p, Qiao G-y, Xiao F-r. Low-Cycle Fatigue Properties of the X70 High-Frequency Electric-Resistant Welded Pipes.*Advances in Materials Science and Engineering.* 2018;2018:1-10.

18. Liu W, Lu F, Yang R, Tang X, Cui H. Gleeble simulation of the HAZ in Inconel 617 welding. *Journal of Materials Processing Technology.*2015;225:221-228.

19. Nishikawa H-a, Furuya Y, Igi S, et al. Effect of microstructure of simulated heat-affected zone on low- to high-cycle fatigue properties of low-carbon steels. *Fatigue & Fracture of Engineering Materials & Structures.* 2020;n/a(n/a).

20. Arora KS, Pandu SR, Shajan N, Pathak P, Shome M. Microstructure and impact toughness of reheated coarse grain heat affected zones of API X65 and API X80 linepipe steels. *International Journal of Pressure Vessels and Piping.* 2018;163:36-44.

21. Mohammadi F, Eliyan FF, Alfantazi A. Corrosion of simulated weld HAZ of API X-80 pipeline steel. *Corrosion Science.* 2012;63:323-333.

22. Ronevich JA, Ju Song E, Feng Z, Wang Y, D'Elia C, Hill MR. Fatigue crack growth rates in high pressure hydrogen gas for multiple X100 pipeline welds accounting for crack location and residual stress.*Engineering Fracture Mechanics.* 2019:106846.

23. Zhao ZP, Qiao GY, Li GP, Yang WW, Liao B, Xiao FR. Fatigue properties of ferrite/bainite dual-phase X80 pipeline steel welded joints. *Science & Technology of Welding & Joining.*2016;22(3):217-226.

24. Zhao Z, Xu P, Cheng H, Miao J, Xiao F. Characterization of Microstructures and Fatigue Properties for Dual-Phase Pipeline Steels by Gleeble Simulation of Heat-Affected Zone. *Materials (Basel).*2019;12(12).

25. Tong M, Di X, Li C, Wang D. Toughening mechanism of inter-critical heat-affected zone in a 690 MPa grade rack plate steel. *Materials Characterization.* 2018;144:631-640.

26. Han YD, Jing HY, Xu LY. Welding heat input effect on the hydrogen permeation in the X80 steel welded joints. *Materials Chemistry and Physics.* 2012;132(1):216-222.

27. Park SH, Lee CS. Relationship between mechanical properties and high-cycle fatigue strength of medium-carbon steels. *Materials Science and Engineering: A.* 2017;690:185-194.

28. Qiu Y, Pang JC, Zou CL, Zhang MX, Li SX, Zhang ZF. Fatigue strength model based on microstructures and damage mechanism of compacted graphite iron. *Materials Science and Engineering: A.*2018;724:324-329.

29. Schijve J. Fatigue as a Phenomenon in the Material. In:*Fatigue of Structures and Materials.* Dordrecht: Springer Netherlands; 2009:13-58.

30. Paris P, Erdogan F. A critical analysis of crack propagation laws. 1963.

31. Zhong Y, Xiao F, Zhang J, Shan Y, Wang W, Yang K. In situ TEM study of the effect of M/A films at grain boundaries on crack propagation in an ultra-fine acicular ferrite pipeline steel. *Acta Materialia.*2006;54(2):435-443.

32. Gu Y, Tian P, Wang X, Han X-l, Liao B, Xiao F-r. Non-isothermal prior austenite grain growth of a high-Nb X100 pipeline steel during a simulated welding heat cycle process. *Materials & Design.*2016;89:589-596.

17

33. Badji R, Chauveau T, Bacroix B. Texture, misorientation and mechanical anisotropy in a deformed dual phase stainless steel weld joint. *Materials Science and Engineering: A.* 2013;575:94-103.

34. Omale JI, Ohaeri EG, Szpunar JA, Arafin M, Fateh F. Microstructure and texture evolution in warm rolled API 5L X70 pipeline steel for sour service application. *Materials Characterization.* 2019;147:453-463.

35. Ju Y-B, Koyama M, Sawaguchi T, Tsuzaki K, Noguchi H. Effects of ε-martensitic transformation on crack tip deformation, plastic damage accumulation, and slip plane cracking associated with low-cycle fatigue crack growth. *International Journal of Fatigue.* 2017;103:533-545.

36. Koyama M, Zhang Z, Wang M, et al. Bone-like crack resistance in hierarchical metastable nanolaminate steels. *Science.* 2017;355(6329):1055.

37. Naragani D, Sangid MD, Shade PA, et al. Investigation of fatigue crack initiation from a non-metallic inclusion via high energy x-ray diffraction microscopy. *Acta Materialia.* 2017;137:71-84.

38. Dahar MS, Seifi SM, Bewlay BP, Lewandowski JJ. Effects of test orientation on fracture and fatigue crack growth behavior of third generation as-cast Ti–48Al–2Nb–2Cr. *Intermetallics.* 2015;57:73-82.

18

(a) Crack propagation direction

100 um

(b) 90 um

(c) 60 um

(111)
(001) (101)
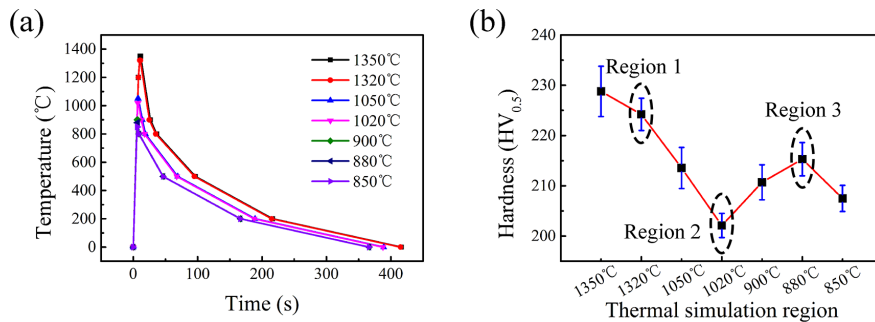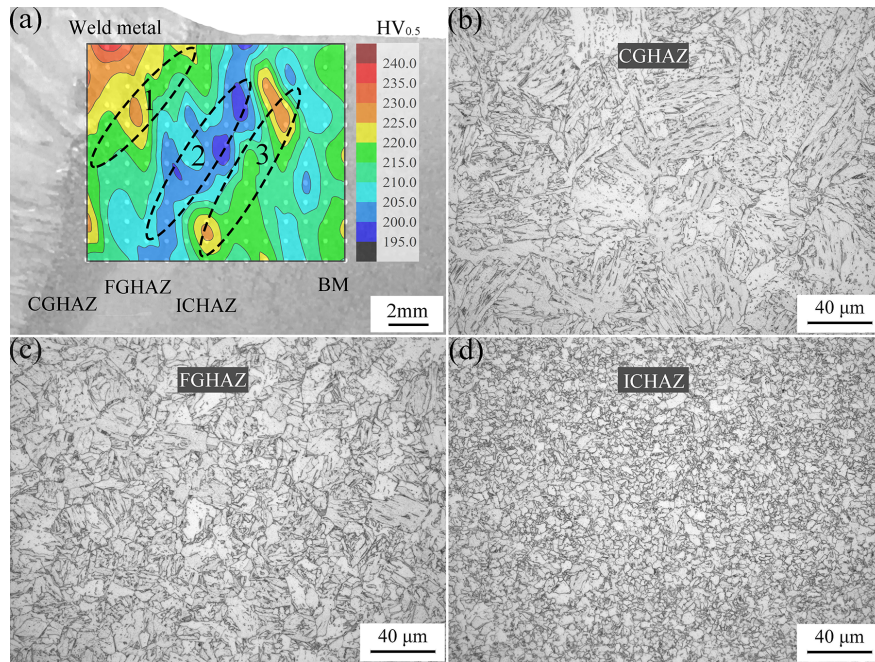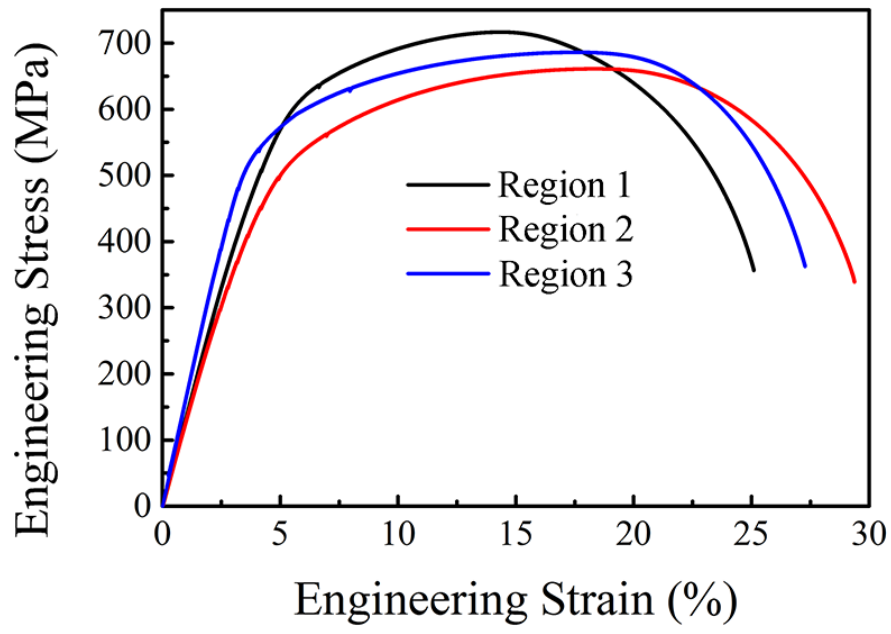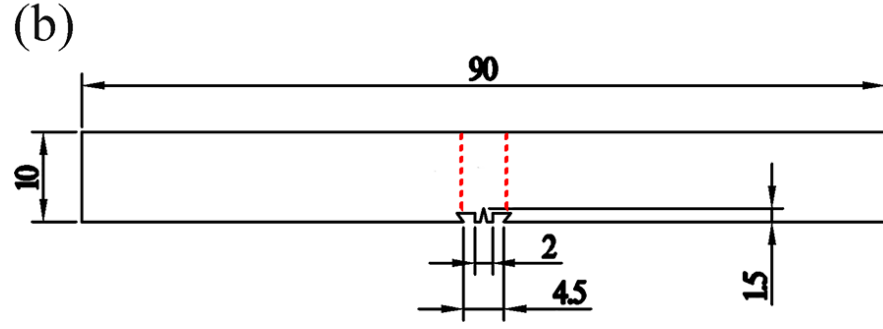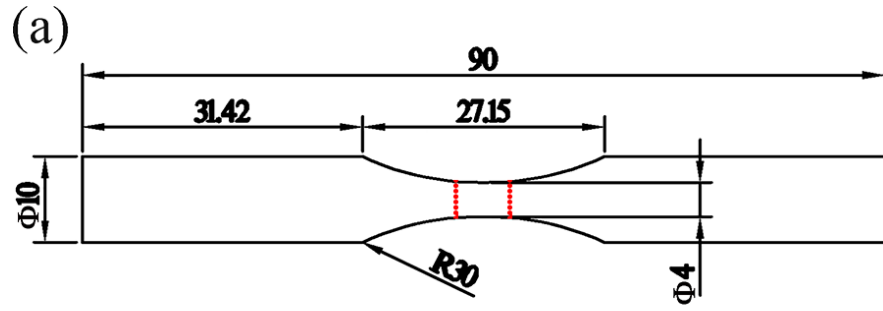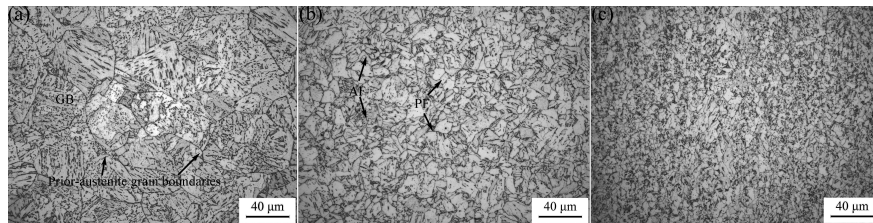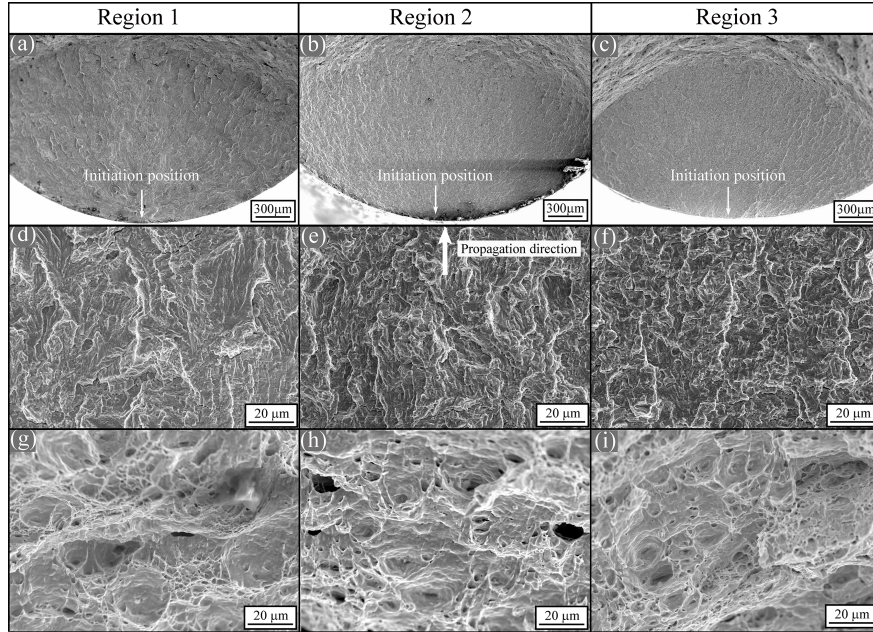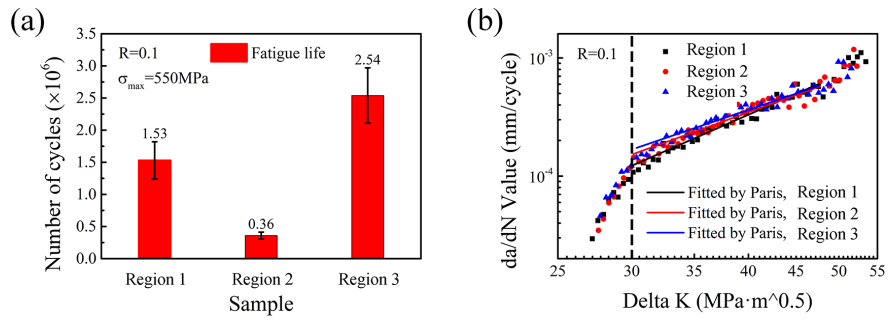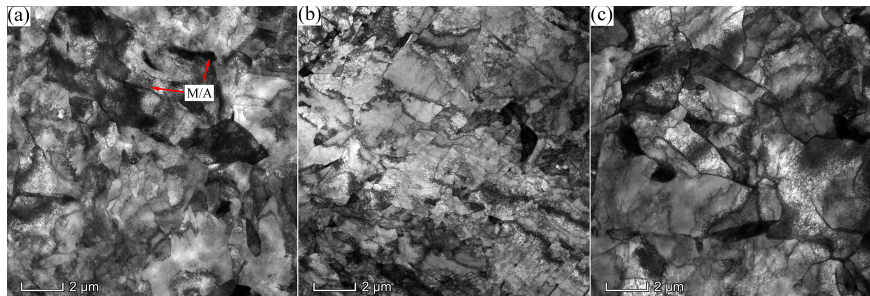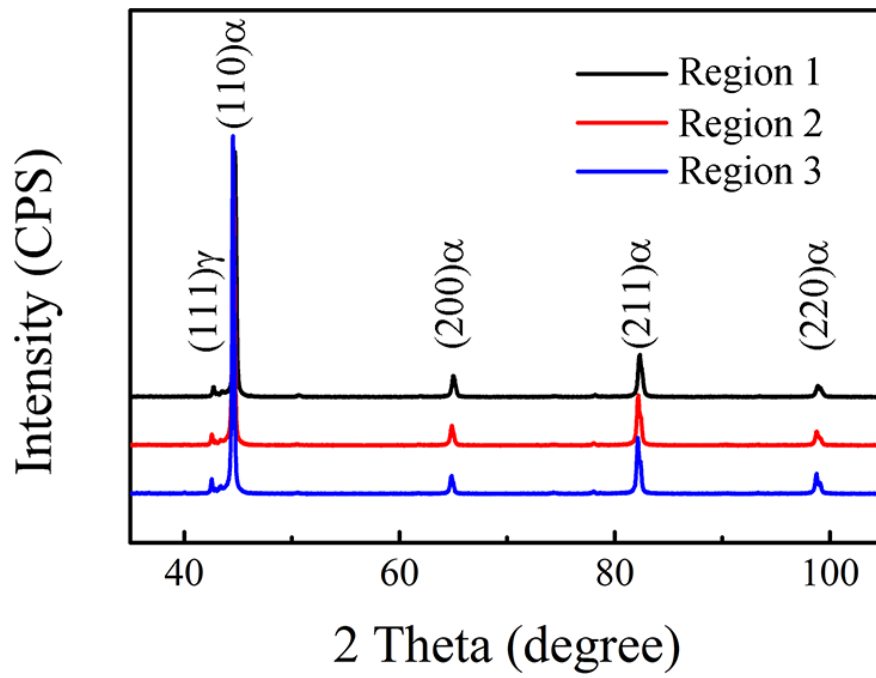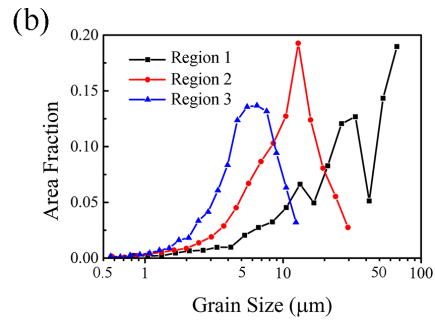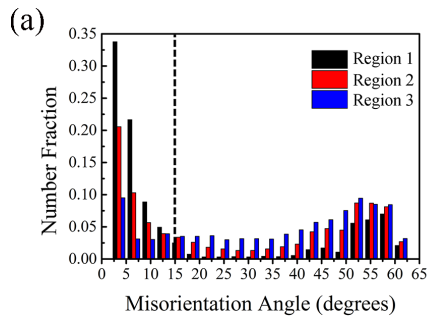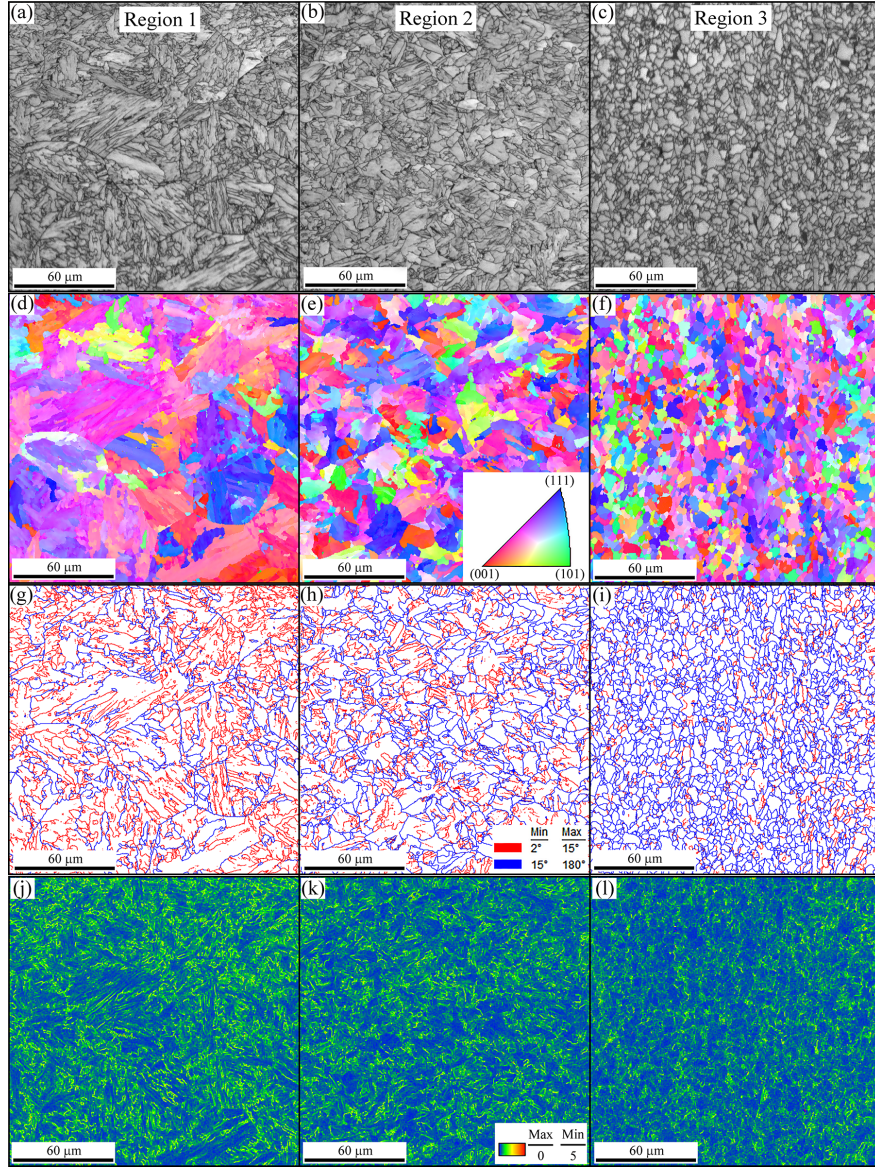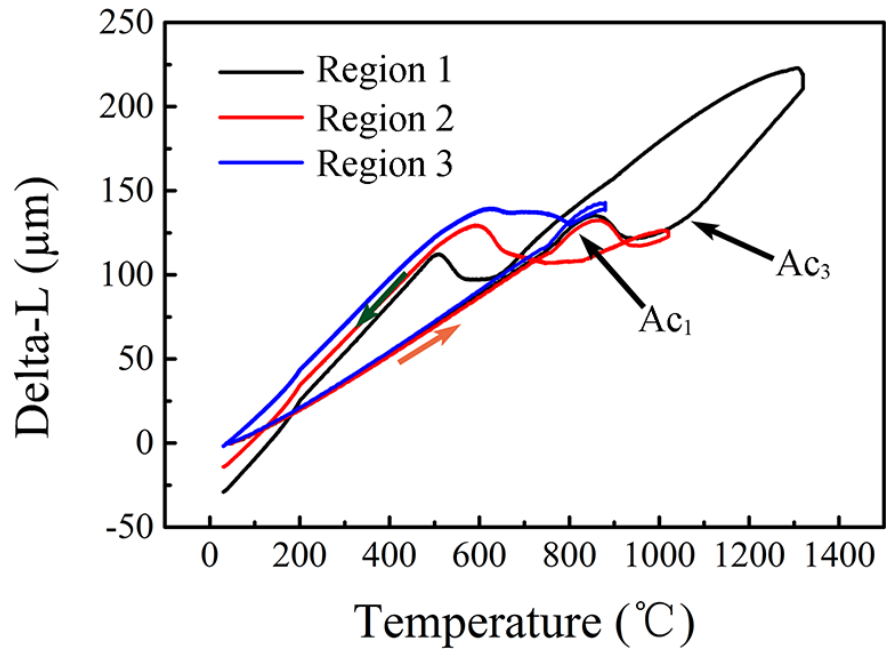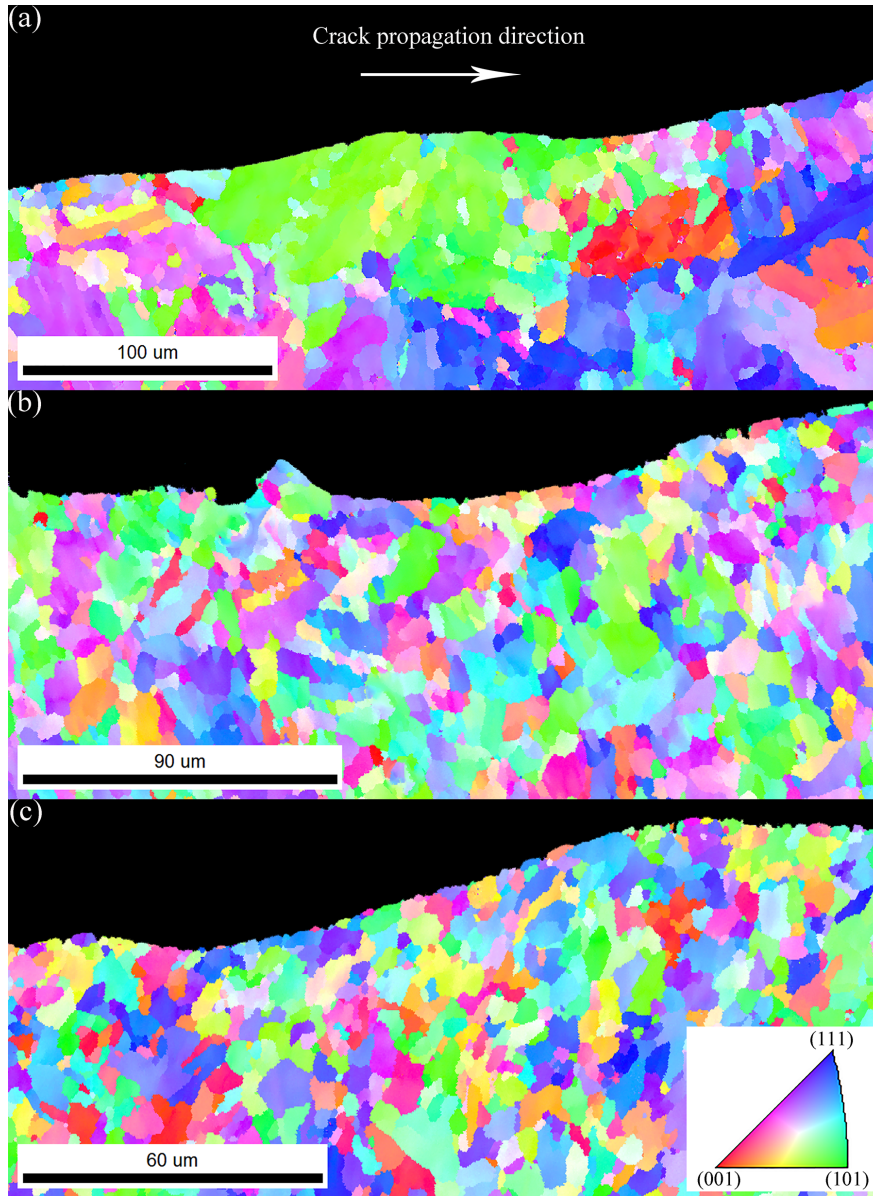
**Hosted file**

Table 1.docx available at https://authorea.com/users/305071/articles/435663-research-on-the-fatigue-properties-of-sub-hazs-in-the-x80-pipe

**Hosted file**

Table 2.docx available at https://authorea.com/users/305071/articles/435663-research-on-the-fatigue-properties-of-sub-hazs-in-the-x80-pipe

**Hosted file**

Table 3.docx available at https://authorea.com/users/305071/articles/435663-research-on-the-fatigue-properties-of-sub-hazs-in-the-x80-pipe